

PAPER • OPEN ACCESS

# Broadband Alfvénic excitation correlated to turbulence level in the Wendelstein 7-X stellarator plasmas






To cite this article: S. Vaz Mendes *et al* 2023 *Nucl. Fusion* **63** 096008

View the [article online](#) for updates and enhancements.

You may also like

- [Alfvén waves in reversed-field pinch and tokamak ohmic plasmas: nonlinear 3D MHD modeling and comparison with RFX-mod](#)  
A. Kryzhanovskyy, D. Bonfiglio, S. Cappello et al.
- [Modification of Alfvén wave dispersion and Alfvén wave heating in multiple ion species tokamak plasmas](#)  
A G Elfimov, R M O Galvão, I C Nascimento et al.
- [Ion Heating from Nonlinear Landau Damping of High Mode Number Toroidal Alfvén Eigenmodes](#)  
T. S. Hahm

# Broadband Alfvénic excitation correlated to turbulence level in the Wendelstein 7-X stellarator plasmas

S. Vaz Mendes<sup>1,\*</sup>, K. Rahbarnia<sup>1</sup> , C. Slaby<sup>1</sup>, H. Thomsen<sup>1</sup>, J. Schilling<sup>1</sup> , M. Borchardt<sup>1</sup>, R. Kleiber<sup>1</sup> , A. Könies<sup>1</sup> , J.-P. Böhner<sup>2</sup>, A. von Stechow<sup>1</sup>, T. Sunn Pedersen<sup>1,3</sup> , T. Klinger<sup>1</sup> and the W7-X Team<sup>a</sup>

<sup>1</sup> Max-Planck-Institute for Plasma Physics, Wendelsteinstr. 1, 17491 Greifswald, Germany

<sup>2</sup> MIT Plasma Science and Fusion Center, Cambridge, MA 02139, United States of America

E-mail: [sara.mendes@ipp.mpg.de](mailto:sara.mendes@ipp.mpg.de)

Received 12 December 2022, revised 20 June 2023

Accepted for publication 7 July 2023

Published 28 July 2023



## Abstract

During the first operational phase (OP1) of the Wendelstein 7-X (W7-X) stellarator, poloidal magnetic field fluctuations,  $B_\theta$ , were measured in several different plasma scenarios with a system of Mirnov coils. In the spectrograms, multiple frequency bands close together in frequency are observed below  $f = 600$  kHz. Furthermore, a dominant feature is the appearance of a frequency band with the highest spectral amplitude centred between  $f = 180 - 220$  kHz. The fluctuations are observed from the beginning of most W7-X plasmas of OP1, which were often operated solely with electron cyclotron resonance heating. The fluctuations show characteristics known from Alfvén waves and possibly Alfvén eigenmodes (AEs). However, the fast particle drive from heating sources, which is generally a driver necessary for the appearance of AEs in magnetic confinement plasmas, is absent in most of the analysed experiments. A characterization of the Alfvénic fluctuations measured during OP1 plasmas is possible using a newly developed tracking algorithm. In this paper, we extensively survey the different spectral properties of the fluctuations in correlation with plasma parameters and discuss possible driving mechanisms. The correlation studies of the dynamics of the possible ellipticity induced AEs indicate that Alfvén activity in the frequency interval between  $f = 100 - 450$  kHz could be excited due to an interaction with turbulence, or profile effects also affecting the turbulence amplitude.

Keywords: stellarator, magnetic fluctuations, Alfvén modes, broadband Alfvénic excitation, Mirnov coils

<sup>a</sup> See Sunn Pedersen *et al* 2022 (<https://doi.org/10.1088/1741-4326/ac2cf5>) for the W7-X Team.

<sup>3</sup> Present address: Type One Energy Group, Madison, WI 53703, United States of America.

\* Author to whom any correspondence should be addressed.



Original Content from this work may be used under the terms of the [Creative Commons Attribution 4.0 licence](https://creativecommons.org/licenses/by/4.0/). Any further distribution of this work must maintain attribution to the author(s) and the title of the work, journal citation and DOI.

## 1. Introduction

The Wendelstein 7-X (W7-X) is an optimized stellarator device located in Greifswald, Germany. Three plasma operation phases (OPs) have been successfully completed between 2015–2018, named OP1.1, OP1.2a and OP1.2b [21, 22]. The results collected so far already proved the optimization of plasma confinement for a HELIAS device (HELical Advanced Stellarator) [21] with reduced neoclassical transport [5] and minimal self-generated plasma currents [26]. W7-X is a reactor relevant experiment and the results from its OPs are part of a great effort in solving some of the biggest challenges in magnetic confinement fusion, and future fusion power plants.

In magnetic confinement plasmas, Alfvén waves (AWs) constitute in general a continuous spectrum of electromagnetic waves [9, 10, 19]. The waves in the continuous spectrum are strongly damped (mainly due to the phase-mixing mechanism [42]). On the other hand, in gaps of the continuum, discrete Alfvén eigenmodes (AEs) that are weakly damped can exist. Those AEs are therefore more easily driven to grow in amplitude [42]. A common driving mechanism of AEs is through resonant wave–particle interactions. The necessary velocities require energetic particle species (EPs), and one ordinarily refers to this mechanism as EP-drive or fast-particle drive of AEs. The experimental observation of AEs, in magnetic confinement plasmas, is therefore reported more during plasma scenarios with EP species produced by external heating systems, such as neutral beam injection (NBI) and ion cyclotron resonance heating (ICRH).

Weakly damped AEs have also been observed in the absence of EPs in different fusion devices [16, 24, 32, 34]. A less prevalent, when compared to EP-drive, but still possible driving mechanism of AEs is, for example, by tapping the free energy associated to the thermal plasma profiles. Another example is the observation of Alfvén modes excited by drift Alfvén turbulence in tokamak plasmas [24], where multi-peaked magnetic fluctuations were observed to last throughout the entire duration of purely ohmic plasmas.

In OP1.2b NBI became available at W7-X [1], with the capability of injecting at maximum 55 keV EPs. For future W7-X OPs, a bigger population of EPs is expected with the combination of the NBI and new ICRH [27] systems. Further destabilization of any pre-existing and weakly damped modes (i.e. driven to grow more unstable) can only be predicted, and if necessary avoided, if the driving mechanism of current observations is investigated first. Resonant wave–particle interactions between the hypothetical EP population of future OPs and the AEs are not excluded as a possible cause for the loss of injected particles and energy in future OPs. Particle and energy losses can also be accompanied by damage of plasma facing components (PFCs). For example, during experiments conducted at the DIII-D tokamak energetic beam ions (approximately 75 keV) have been used to further destabilize toroidicity induced AEs (TAEs), and causing the loss of 70% of the injected power for strong TAE mode activity [11]. The

effect of AWs on the confinement of EPs is a common subject of investigations at differing fusion experiments, for both tokamaks [14, 30, 36, 37] and stellarators [18, 25, 28].

This paper presents an extensive survey of Alfvénic modes observed in W7-X plasmas in OP1.2b. AW signatures were detected by multiple fast diagnostics. The Mirnov coil signals measuring the poloidal magnetic field fluctuations have been analysed. Multiple fluctuation bands in the spectrogram of magnetic fluctuations between 100–450 kHz were observed from the beginning of most W7-X ECR heated plasmas. The fluctuation bands show a broad width from about  $\Delta f = 20 - 100$  kHz. Within these multiple bands, one band centred between  $f = 180 - 220$  kHz often displays the highest amplitude. The discharge-lasting appearance of the fluctuation bands in many experimental plasma configurations motivated the development of an algorithm tracing the highest amplitude band. This way the temporal spectral dynamics (frequency and amplitude) of the fluctuations bands through the entire length and in different phases of the plasma can be determined.

Previous reports from experiments at W7-X (in [32, 34]) indicated that the fluctuation bands centred between 170–200 kHz are associated with ellipticity and/or helicity induced gaps of the AW continuum spectrum calculated with CONTI [23]. We note, that Alfvén modes between 170–200 kHz are observed during W7-X ECRH-only plasmas, and therefore fast ion drive cannot explain the activity in this frequency range.

After the findings reported in [32, 34] it remains essential to further investigate the driving mechanism of the Alfvén fluctuation bands that were so common during the W7-X ECR-heated plasmas of OP1.2b. A closer look to the conditions of enhanced and suppressed activity is necessary, followed by determining the correlation between the Alfvénic fluctuations and the plasma general parameters. The results regarding the correlation between the dynamics of the observed AWs and the general plasma parameters can be helpful to explain the initial driving mechanism of the AWs and potentially mitigate them.

In section 3 we introduce a new method to determine how the Alfvén fluctuation bands between  $f = 100 - 450$  kHz develop during different experimental conditions, after a description of the experimental set-up of W7-X diagnostics used in section 2. Section 4 summarizes the main experimental observations, where we find in particular how the spectral properties of the fluctuation bands correlate to different plasma scenarios. In section 5, a discussion on the driving mechanism follows, and the final conclusions are presented in section 6.

## 2. Experimental set-up

The detection and characterization of Alfvénic activity at W7-X is done essentially using the data from the Mirnov diagnostic. The diagnostic consists of a total of 125 spatially distributed coils [13]. The coils are placed at several locations of the vessel wall, where the majority of them are part of poloidal

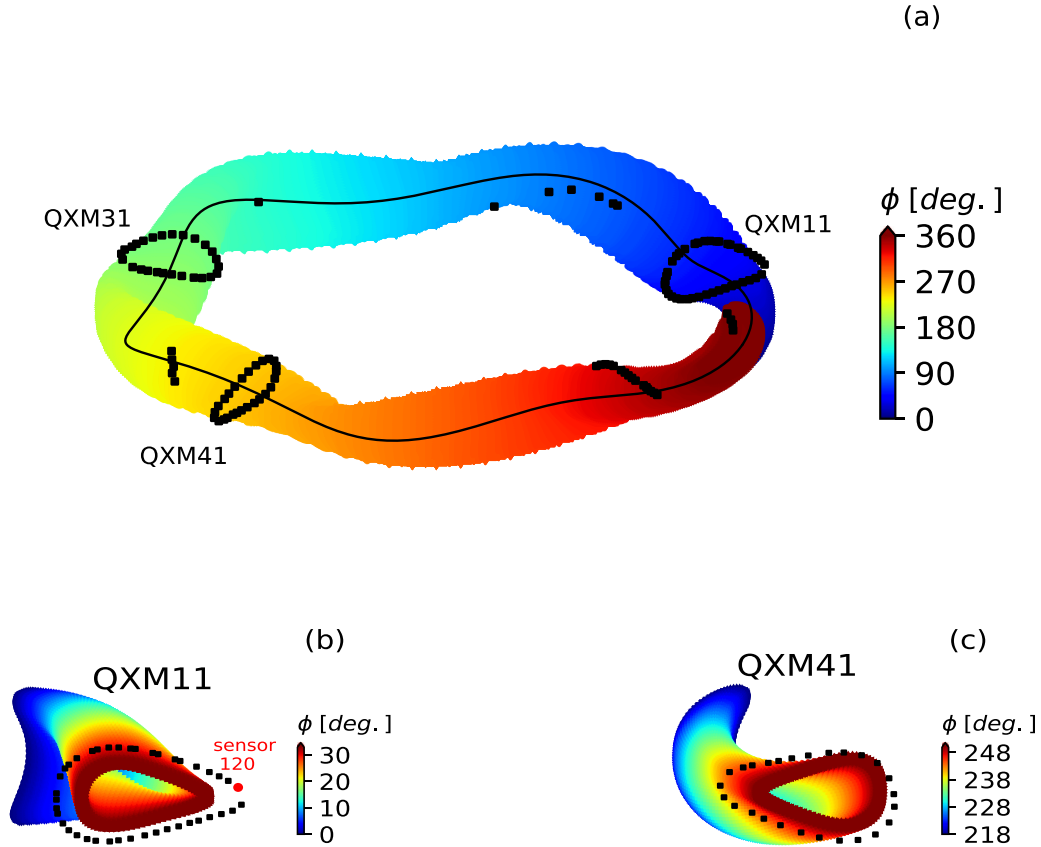


**Figure 1.** (a) Toroidal location ( $\phi$ ) of the 125 Mirnov coils system in a 3d view from above. Poloidal arrays QXM31, QXM11 and QXM41 are arranged in triangular-shaped cross-sections, with up to 41 coils. Smaller coil sets are located on the inboard and outboard sides near bean-shaped cross sections (4–8 coils). (b) Poloidal array QXM11 with sensor QXM11-120 (QXM11CE120). (c) Poloidal array QXM41.

arrangements, see figure 1. Mirnov coils measure the magnetic fluctuations  $dB(t)/dt$  ( $\dot{B}(t)$ ). Their technical realization in this particular experiment allows AC fluctuations above 1 kHz to be measured, with sampling frequency  $f_s = 2$  MHz. The coils are oriented in order to measure the poloidal magnetic field fluctuations ( $\dot{B}_\theta(t)$ ). The maximum voltage that can be induced is of the order of  $\Delta V \simeq 1$  V. The coils cover a frequency range of 1–800 kHz, and mode resolutions for  $m$  up to  $m \simeq 20$  and  $n$  up to  $n \simeq 10$ . The more dominant frequencies in the power spectrum of  $\dot{B}_\theta$  are below 10 kHz, and are caused by the data acquisition system (DAQ) noise signal. A noise component below  $f = 5$ –10 kHz is constant for the Mirnov diagnostic channels in the absence or presence of plasma. The discrimination between plasma related fluctuations and the DAQ intrinsic noise signal becomes increasingly harder below 10 kHz. For higher frequencies, the signal-to-noise ratio (SNR) is less significant, and a well distinguished DAQ artefact is expected at 500 kHz.

To circumvent this problem, the detection of the dominant frequency band (DFB) among the close frequency bands (CFBs) is focused on the range between 100–450 kHz. Further details of the commissioning of the W7-X Mirnov diagnostic are found in [13], which includes a description of the coils composition, technical realization and DAQ. A correlation analysis between the amplitude of the poloidal

magnetic field fluctuations and different heating schemes, magnetic configurations, and plasma parameters is considered. Line integrated plasma electron density measurements ( $\int n_e dl$ ) are obtained from an interferometer diagnostic [8]. The plasma stored energy is proportional to the diamagnetic energy measurements ( $W_{\text{dia}}$ ).  $W_{\text{dia}}$  is measured by diamagnetic loops around the vessel [31]. The electron temperature measurements ( $T_e$ ) are from a central channel of the ECE diagnostic [40], while line integrated ion temperature measurements ( $T_i$ ) are obtained from an x-ray crystal imaging spectrometer diagnostic (XCIS) [29] (using a central channel). The net toroidal current ( $I_{\text{tor}}$ ) is obtained from measurements of the Rogowski coil system [26]. Finally, line-integrated density fluctuations ( $\int \tilde{n}_e dl$ ) throughout the entire plasma cross-section are measured with the Phase Contrast Imaging (PCI) diagnostic [12, 17]. PCI provides a good measurement of the broadband turbulent density fluctuations across a large part of the turbulence wave number spectrum, which are integrated over to compute the displayed fluctuation amplitude. A large part of the fluctuations can be localized radially to the location of the electric field well [2], which tends to be in the region  $r/a = 0.6$ –0.8. The amplitude of the PCI fluctuations will be used to illustrate the turbulence levels throughout the entire plasma cross-section and across a large part of the turbulence wave number spectrum.

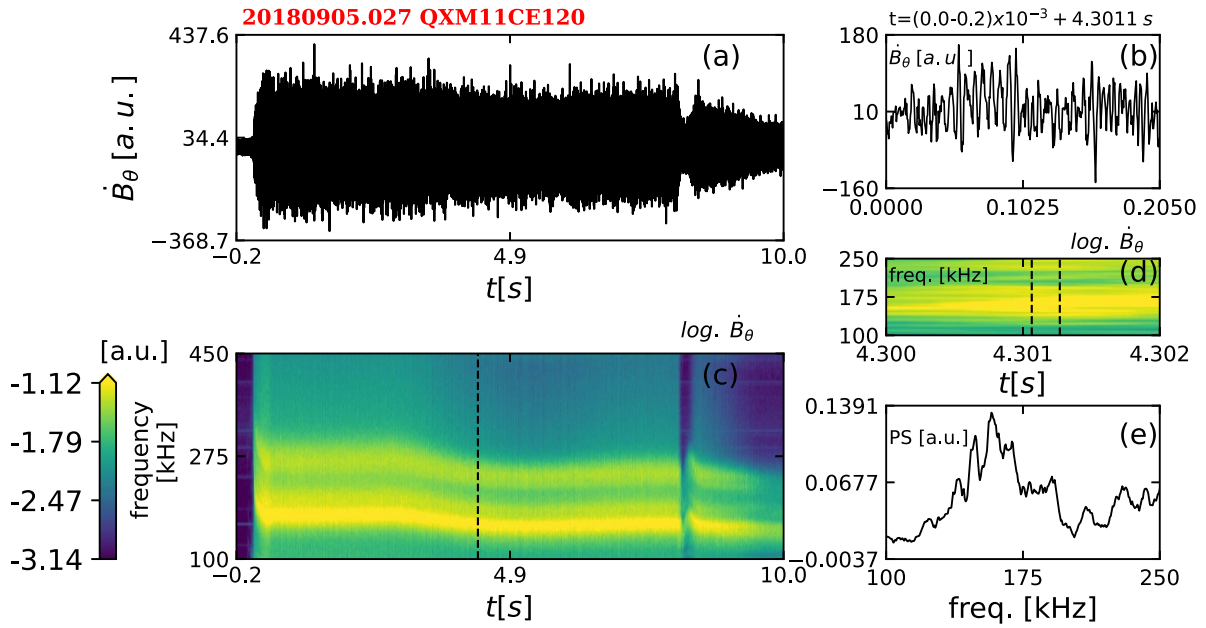


**Figure 2.** (a) Example of the raw  $\dot{B}_\theta$  measurement, using sensor 120 from the QXM11 array. (b) Zoom of  $\dot{B}_\theta$  for  $t = 4.3011 - 4.3013$  s. (c) Spectrogram of the  $\dot{B}_\theta$  signal in (a). (d) Zoom of the structure of the spectrogram for  $t = 4.3011 - 4.3013$  s and  $f = 100 - 250$  kHz. (e) Power spectrum for  $t = 4.3011 - 4.3013$  s, displaying a multi-peaked envelope structure between 100–250 kHz.

### 3. Data evaluation techniques

#### 3.1. Tracking algorithm—for Alfvén fluctuation bands

Figure 2 shows an example of the fluctuating  $B_\theta$  measurements during a W7-X experiment, a spectrogram of  $\dot{B}_\theta$ , and the multi-peaked structure of the fluctuations spectrum. Mainly two broad frequency bands are observed throughout the duration of the plasma (in the spectrogram of figure 2(c)). The  $\dot{B}_\theta$  spectrograms during OP1.2b often reveal multiple broad bands with widths between  $\Delta f \simeq 20$  to  $\Delta f \simeq 100$  kHz.

A tracking method has been developed in order to extract the temporal dynamic of the one band with the highest power spectral density (PSD), named the DFB. In figure 3(f), the outcome of the method is shown for the example spectrum in figure 3(a).

The goal of the method is to determine the local maximum PSD values within different  $\Delta t_l$ -windows, and also within different frequency windows  $\Delta f_k = 5$  kHz. In figures 3(b)–(e) the PSD maximum values extracted are represented for different frequency windows  $\Delta f_k$  by different colours. For each  $\Delta t_l$  a threshold,  $A_{\text{thresh}}^l$ , is defined in order to distinguish and extract the dominant features of the spectrogram in that time window. The maximum PSD values are found when the average of the points in a specific  $\Delta f_k$  window is above the threshold.

The frequencies that correspond to the maximum values in each  $\Delta t_l$ ,  $\Delta f_k$  window are represented by  $f_{\text{DFB}}^{kl}$ . All the  $f_{\text{DFB}}^{kl}$  vectors evaluated for the entire time and frequency domain of the spectrogram in figure 3(a) are joined into the M, N-dimensional  $f_{\text{DFB}}(t)$  band, as illustrated from figure 3(d) to an instance of 3(f). In figure 3(f) the final result for the example in figure 3(a) is shown. The respective amplitude of the final DFB result over time is shown in grey scale.

We note, that for certain periods (e.g. from  $t = 1.5$  s to  $t = 1.9$  s or again after  $t = 3.7$  s) two or more frequency bands with high PSD amplitudes are found in the same time range, leading to an apparent dithering of the determined DFB. This is caused by two separated peaks in the distribution with amplitudes above the threshold  $A_{\text{thresh}}^l$ . This type of ambiguity when trying to resolve a single DFB is yet to be eliminated automatically and is for now resolved by manual inspection. More details on the implementation can be found in [appendix](#).

### 4. Detection of discharge lasting Alfvénic modes between 100–450 kHz

During OP1.2b multiple CFBs were commonly observed in the spectrograms of magnetic fluctuations below 600 kHz. We define the CFBs to consist of frequency bands with widths between  $\Delta f \simeq 20 - 100$  kHz, where adjacent bands are not separated by more than 100 kHz. The frequencies of the individual bands change in a correlated way within the CFBs. The time evolution of the central frequency of the different CFBs is identical and scales with the Alfvénic speed  $v_A \propto \frac{1}{\sqrt{n_e}}$  in most experimental phases of OP1.2b. In some examples pairs of adjacent CFBs can be separated (in frequency space) by small distances starting from 5 kHz, while in other examples separations of up to 100 kHz are observed. The CFBs frequently constitute of 2–4 bands in the frequency range of the  $\dot{B}_\theta$  spectrograms. The individual CFBs are observed throughout the entire duration of most discharges. They are therefore a discharge-lasting feature in most W7-X plasmas. A dominant feature is the appearance of a DFB with its centre between  $f = 180 - 220$  kHz. Changes in the frequency width,

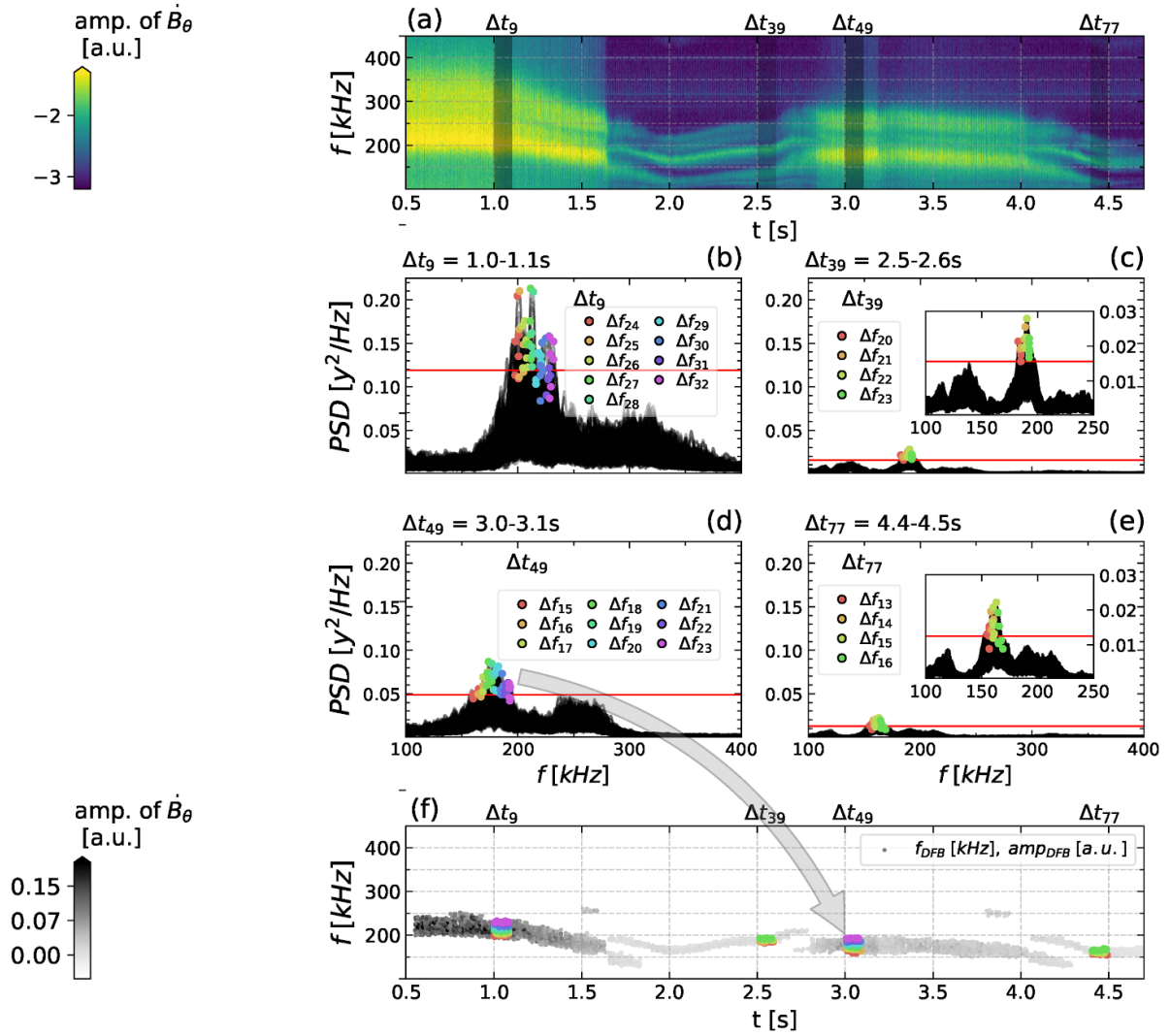


**Figure 3.** (a) Spectral analysis of the signal of Mirnov coil QXM11CE120 for experimental discharge #20180809.039. (b)–(e) Examples of the 2049 PSD calculations during four temporal windows of the Spectrogram in (a). For each  $\Delta t_l$ , a tracking algorithm determines maximums for different frequency intervals  $\Delta f_k$ , shown by the different coloured circles. Thresholds to determine the maximums are represented by the red lines. (f) Representation of the entire  $f_{\text{DFB}}(t)$  result of the tracking method (black circles). The amplitude,  $A_{\text{DFB}}(t)$  [a.u.], corresponds to the intensity of the circles.

and amplitude signals of the CFBs are well represented by the properties of the DFB ( $\Delta f_{\text{DFB}}$  and  $A_{\text{DFB}}$ ).

The spectrograms in figures 4(a)–(c) show examples of very similar CFBs observed during the W7-X experimental discharges #20181009.010, #20181011.010 and #20180809.039, respectively. Figures 5(a)–(c) show an overview of the standard plasma parameters during those experimental programs. We note that the three experimental programs shown were conducted on different days.

The frequency of the DFB ( $f_{\text{DFB}}(t)$ ) was determined for these three examples with the tracking algorithm between  $f = 100 - 450$  kHz. The  $f_{\text{DFB}}(t)$  signals are shown by the black circles in figures 5(a)–(c) (bottom row). Sometimes the  $f_{\text{DFB}}$  signals in figures 5(b) and (c) do not follow the  $\frac{1}{\sqrt{n_e}}$  scaling (indicative of an Alfvénic nature of the observed CFBs / DFBs) very well. A possible reason for this observation is that

the comparison is to the line-averaged density while the mode activity related to the DFB is most likely localized. The local radial density  $n_e(r_{\text{AW}})$  at the radius of the AW could change without altering the line-averaged density.

The width of the DFB,  $\Delta f_{\text{DFB}}$ , is estimated from the extracted  $f_{\text{DFB}}(t)$  signals. The amplitude of the DFB ( $A_{\text{DFB}}(t)$ ) is represented by the intensity of the circles (in a.u.). We note that in figures 5(b) and (c) more than one band with high PSD is extracted in some time intervals, despite the initial goal to track a single DFB in most intervals.

#### 4.1. Frequency bands width dynamics

Two distinct CFBs are observed between  $f \simeq 200 - 300$  kHz consistently across different heating and plasma scenarios (cf figures 4(a)–(c) and 5(a)–(c)).

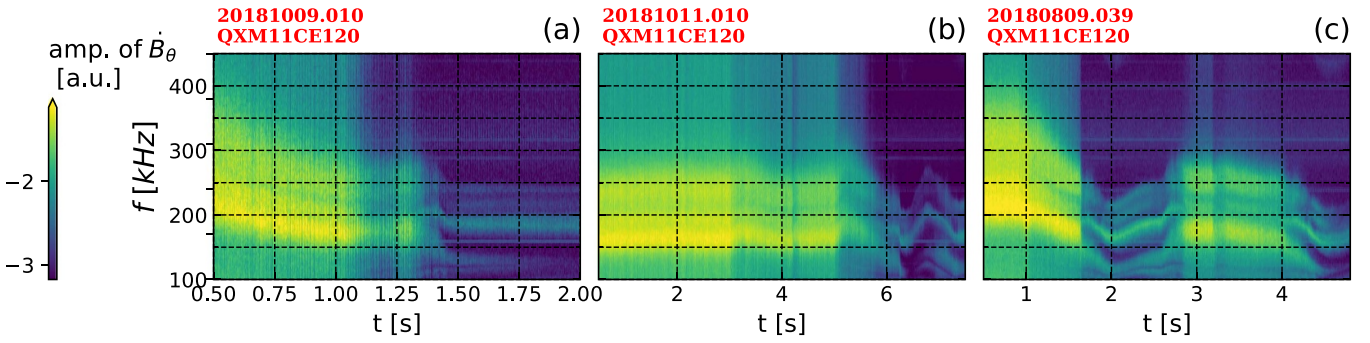


**Figure 4.** Spectral analysis of the signal of Mirnov coil QXM11CE120 for three experimental discharges: (a) #20181009.010, (b) #20181011.010 and (c) #20181016.039 (same as in figure 3).

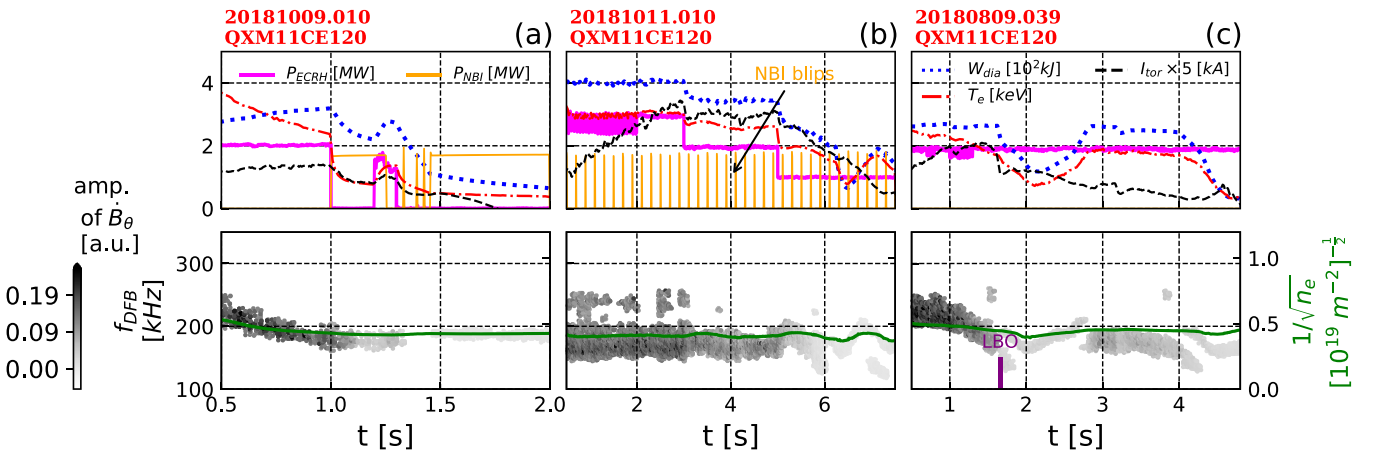


**Figure 5.** Standard plasma parameters during discharges #20181009.010 (a), #20181011.010 (b), and #20181016.039 (c). Top row: time series of the powers of the heating sources, ECRH,  $P_{\text{ECRH}}$  (magenta), and NBI,  $P_{\text{NBI}}$  (orange), plasma diamagnetic energy  $W_{\text{dia}}$  (blue), electron temperature  $T_e$  (red), and a scaling of the net toroidal current  $I_{\text{tor}}$  (black); bottom row: time trace of the DFB,  $f_{\text{DFB}}(t)$  (black circles), and line integrated plasma density,  $\int n_e dl$  (green). The amplitude of the DFB is shown in grey scale.

In the #20180809.039 discharge, a strong plasma perturbation is caused after an intense laser blow-off injection [39] of impurity (Fe/Ti) at  $t = 1.660$  s. The plasma perturbation results in a transient strong reduction of the plasma diamagnetic energy measurement, with  $\Delta W_{\text{dia}} \sim 100$  kJ and  $W_{\text{dia}}$  below 200 kJ. In this time window, narrower CFBs with  $\Delta f_{\text{DFB}} \lesssim 50$  kHz are also clearly visible (cf figure 5(c)).

The different CFBs can be distinguished by the different multi-peaked envelope structures in the PSD functions in figures 3(b)–(e). The PSD functions for  $t = 1.0 - 1.1$  s in figure 3(b) and  $t = 3.0 - 3.1$  s in figure 3(d) have broader envelope structures, while for  $t = 2.5 - 2.6$  s in figure 3(c) and  $t = 4.4 - 4.5$  s in figure 3(e) narrower envelope structures are observed. In the examples of figures 5(a) and (b) changes in  $W_{\text{dia}}$  are introduced by lower ECR heating causing lower electron plasma temperatures. We note that the plasma breakdown and initial heating was always with ECRH-only. The widths of the CFBs for the example in figures 4(a) and 5(a) are almost the same up to  $t = 1$  s, and starts decreasing as  $W_{\text{dia}}$  decreases after  $t = 1$  s. A more drastic change for  $\Delta f_{\text{DFB}} \lesssim 50$  kHz seems to be correlated to the fall of  $W_{\text{dia}}$  below 200 kJ after  $t \simeq 1.5$  s. Moreover, during the brief increase of  $W_{\text{dia}}$  at  $t \simeq 1.25$  s,  $\Delta f_{\text{DFB}}$  briefly increases as well. The individual CFBs visible

in figure 4(b) also become much narrower after a decrease of  $W_{\text{dia}} \lesssim 200$  kJ after  $t = 6$  s.

#### 4.2. DFB amplitude dynamics

During OP1.2b the DFB was typically observed below 450 kHz in Mirnov data.

In figures 6(a)–(c) are depicted the standard plasma parameters introduced in the overview in figure 5(b) for discharge #20181011.010. Added is also the amplitude of line integrated density fluctuations,  $\int \tilde{n}_e dl$  [ $\text{m}^{-2}$ ], in figure 6(d). The moving average of the amplitude of the Alfvén DFB is represented in figure 6(d) by the red line, while  $\int \tilde{n}_e dl$  was represented by the black line in the same figure. During this example the ECR heating decreases in power steps, causing decreasing steps in  $T_e$ , and also decreases in  $W_{\text{dia}}$ . We observe that the time-averaged amplitude of the Alfvénic DFB decreases with the ECRH steps until approximately  $t = 5.5$  s in figure 6(d).

The amplitude of turbulent density fluctuations ( $\int \tilde{n}_e dl$ ) follows the decreasing steps of  $T_e$ . This behaviour has also been reported for a similar scenario with ECRH power steps and a relation to the ITG mode instability limit has been proposed

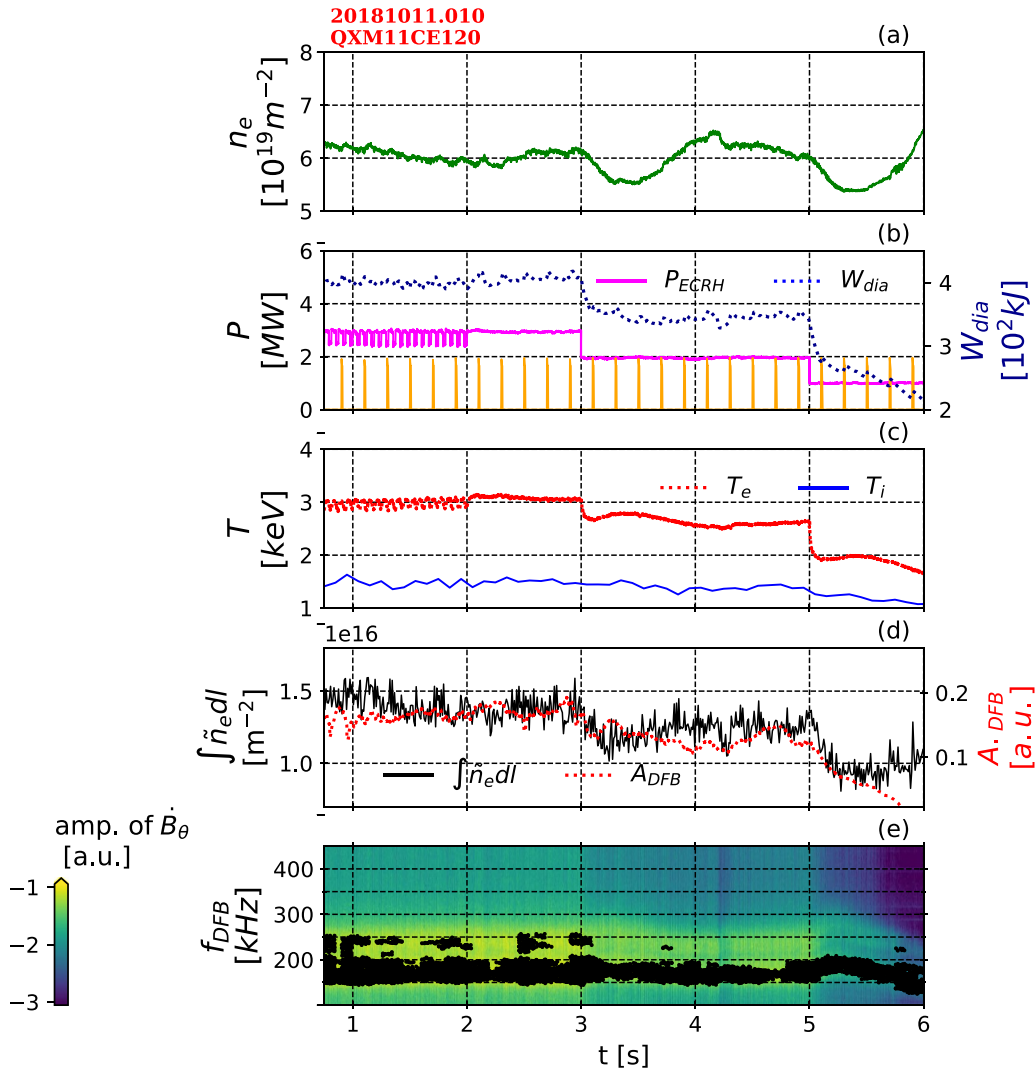


**Figure 6.** (a) For experimental discharge #20181011.010, line-averaged density,  $\int n_e dl$  (green). (b) Heating powers,  $P_{ECRH}$  (magenta) and  $P_{NBI}$  (orange), and diamagnetic energy,  $W_{dia}$  (blue). (c)  $T_e$  (red) and  $T_i$  (blue). (d) Processed data from channel 16 of the PCI diagnostic, indicative of the amplitude of turbulent density fluctuations  $\int \tilde{n}_e dl$  (black), and the moving average of the amplitude of the Alfvén DFB,  $A_{DFB}$  (red). (e) Spectrogram of  $\dot{B}_\theta$  with the Alfvén DFB,  $f_{DFB}(t)$ , depicted by the black circles.

[38]. ITG instabilities that govern turbulence in W7-X plasmas are characterized by a growth rate that in many regimes of interest depends on the temperature ratio  $T_i/T_e$  [35, 38]. Lower growth rates of ITG turbulence are expected for each decreasing step of  $T_e$  with the changes in the temperature ratios (without alterations on neither the normalized gradient lengths of  $n_e$  nor  $T_{e,i}$ , [38]).

This example in figure 6 shows how we can now easily correlate the properties of the dominant Alfvénic modes to general plasma parameters during the duration of entire W7-X discharges.

#### 4.3. Correlation of DFB dynamics with general plasma parameters

Similar to the comparison between  $f_{DFB}(t)$  and  $A_{DFB}(t)$  depicted in the first example of figure 6 we perform this integral analysis over many discharges. We use a total of  $N \simeq$

1235 different time points from more than 700 discharges of OP1.2b, with focus on intervals with more steady (plateau) phases of energy and density.

In figure 7 one can see the correlations between the dominant frequency and plasma density, and with the magnetic configuration dependency in color code. The  $f_{DFB}$  experimental trend in figure 7 shows a  $\frac{1}{\sqrt{n_e}}$  dependency as expected for Alfvén waves (which is represented by the red line). The DFB points corresponding to the DBM configuration lie systematically higher than the points from all other magnetic configurations. We focus on four data points from different configurations with similar line integrated density values, indicated in figure 7. The examples marked are for the FTM (high-iota), EJM (standard), DBM (low-iota) and KJM (high-mirror) configurations. AW continuum spectra are calculated with the CONTI code [23] for the conditions of the marked points. The results are shown in figure 8. The centre of the DFBs are plotted as blue lines for the four magnetic



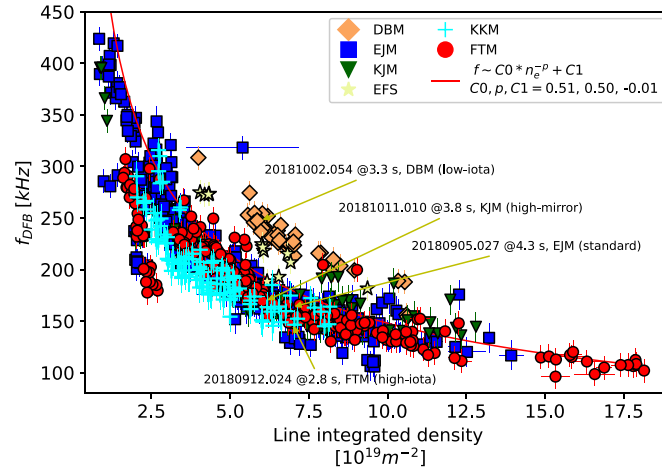


**Figure 7.** Frequency of the Alfvén DFBs,  $f_{\text{DFB}}$ , versus  $\int n_e dl$ , for different magnetic configurations. The configurations considered are listed. The majority of experiments shown here were performed in the EJM (standard) configuration. The standard deviation of the two parameters, at each time point, are represented by the error bars.

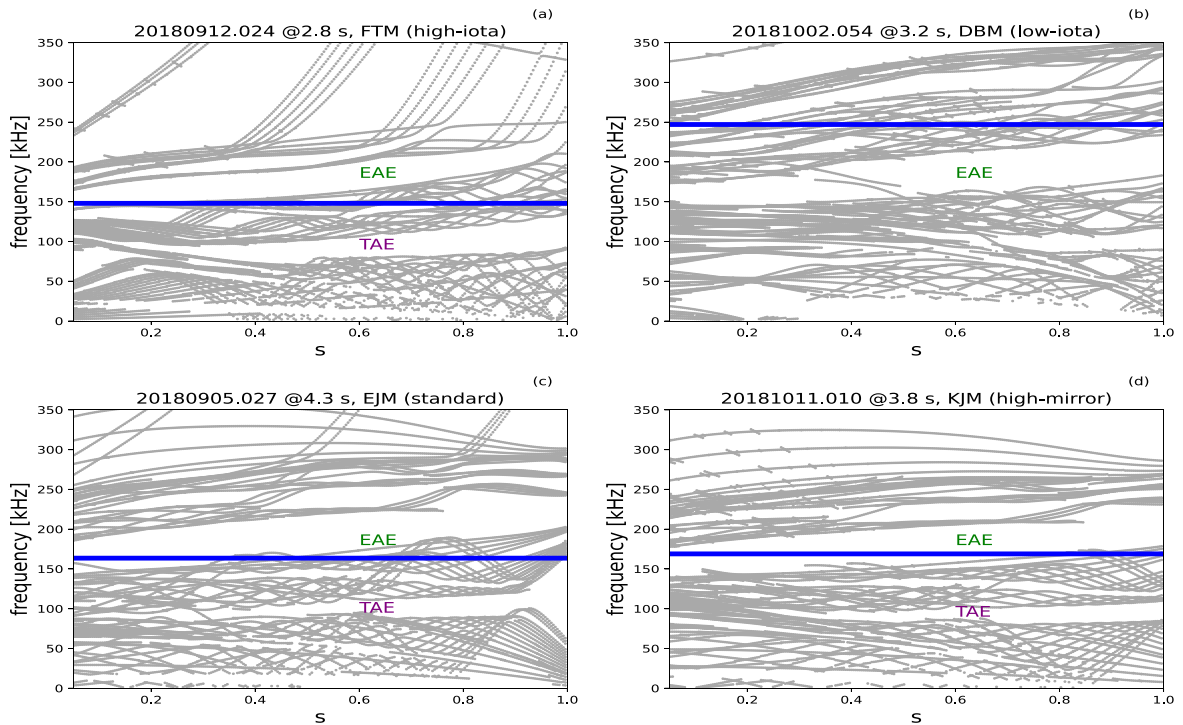


**Figure 8.** (a) Alfvén continuum computed with the code CONTI for a discharge in the EJM (standard) magnetic configuration. (b) in the FTM (high-iota) configuration. (c) in the DBM (low-iota) configuration. (d) in the KJM (high-mirror) configuration. The EAE, and TAE gaps of the Alfvén continuum are labelled. The frequency of the DFB determined from the experimental  $\dot{B}_\theta$  signals are plotted by the blue lines.

configurations. The rotational transform (iota) for the respective configurations are shown in figure 9.

The amplitude of the DFBs are compared to the ECRH power and diamagnetic energy in figure 10. The amplitude trends of the DFB show a configuration dependency for both  $P_{\text{ECRH}}$  and  $W_{\text{dia}}$ . We find that the amplitudes of the DFBs are positively correlated to the ECR heating power as well as the plasma stored energy. For the different magnetic

configurations, the curves of  $A_{\text{DFB}}$  as a function of  $P_{\text{ECRH}}$  and  $W_{\text{dia}}$  surpasses a linear trend. The amplitudes in the FTM configuration are in general distinctively higher for most experiments analysed (red circles). We note, that some  $A_{\text{DFB}}$  values of the FTM configuration are below  $A_{\text{DFB}} = 0.1$  [a.u.] for higher ECRH powers between  $P_{\text{ECRH}} \sim 4 - 6$  [MW] in figure 10(a). These  $A_{\text{DFB}}$  values correspond to experiment phases with high plasma radiated power.

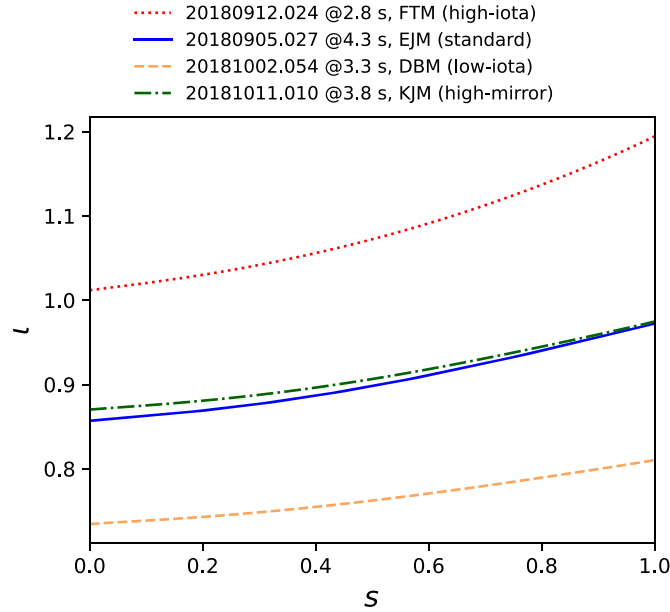


**Figure 9.** Iota profiles for the Alfvén continuum computations shown in figure 8 obtained with VMEC.

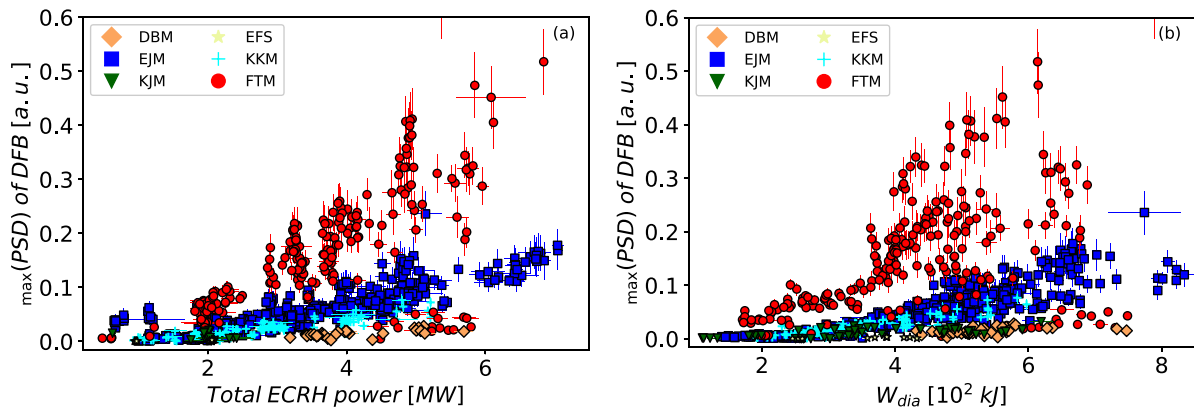


**Figure 10.** (a) Amplitude of the Alfvén DFBs,  $A_{\text{DFB}}$ , versus  $P_{\text{ECRH}}$ . (b)  $A_{\text{DFB}}$  versus  $W_{\text{dia}}$ , indicative of the plasma stored energy. The data is taken for different magnetic configurations of W7-X, as listed in the legend. The standard deviation of each parameter, at each time point, is represented by the error bars.

In figure 11 we plot the amplitude of the DFBs versus the turbulence level. A positive correlation is found for all configurations with the exception of the KJM.

#### 4.4. Deviation from the amplitudes scaling with ECRH power and plasma energy

The example in figure 12 corresponds to a pellet fuelling experiment, during which frozen hydrogen pellets have been injected into the plasma [3].

The pellets were injected at about  $t_1 = 1.6$  s until  $t_2 = 2.4$  s (visible as large spikes of the turbulence level). The plasma stored energy peak-value between  $t_3$  and  $t_4$  marks a high performance (HP) phase of the plasma, with  $W_{\text{dia}} > 1$  MJ. The HP phase is thought to be related to a reduction of the turbulence level due to a peaking of the density profile [4, 6, 35].

At  $t_R$  the large-scale perturbations by the pellets in the  $\int \tilde{n}_e dl$  signal disappear after the last injection at  $t_2$ . With

respect to the level of  $\int \tilde{n}_e(t_R) dl$ , where the pellets do not artificially increase the turbulence level, a reduction of the turbulence is observed from  $t_R$  to  $t_3$ .

For this example we note that  $A_{\text{DFB}}$  decreases for the window of reduced turbulence despite an increase in  $P_{\text{ECRH}}$  and  $W_{\text{dia}}$ , between  $t_R$  and  $t_3$ . This is an exception to the previous findings that  $A_{\text{DFB}}$  scales with  $P_{\text{ECRH}}$  and  $W_{\text{dia}}$ , but nevertheless  $A_{\text{DFB}} \propto \int \tilde{n}_e dl$ . In the preceding section where we analyse the correlation between the DFB dynamics with general plasma parameters we did not include transient intervals such as the HP-phase of pellet fuelling experiments.

A peak in  $\int \tilde{n}_e dl$  before the end of the HP phase is observed between  $t_3$  and  $t_4$ . This peak in the PCI fluctuation amplitude does not stem from the broadband density turbulence, but rather from a frequency-localized mode around  $f = 20 - 50$  kHz also seen in the amplitude of the magnetic fluctuations in the same frequency range. The characterization and/or identification of this particular mode seen in PCI and Mirnov data

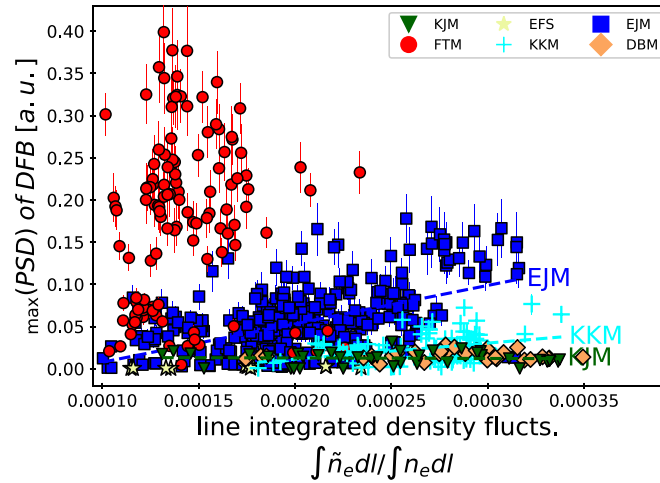


**Figure 11.** Amplitude of the Alfvén DFBs,  $A_{DFB}$ , versus the turbulence level, which is depicted by the line integrated density fluctuations,  $\int \tilde{n}_e dl$  ( $m^{-2}$ ). It is represent  $\int \tilde{n}_e dl$  divided by the line integrated density  $\int n_e dl$  ( $m^{-2}$ ). Linear regressions are adjusted for the data points of configurations with more measurements (EJM, KKM and KJM).

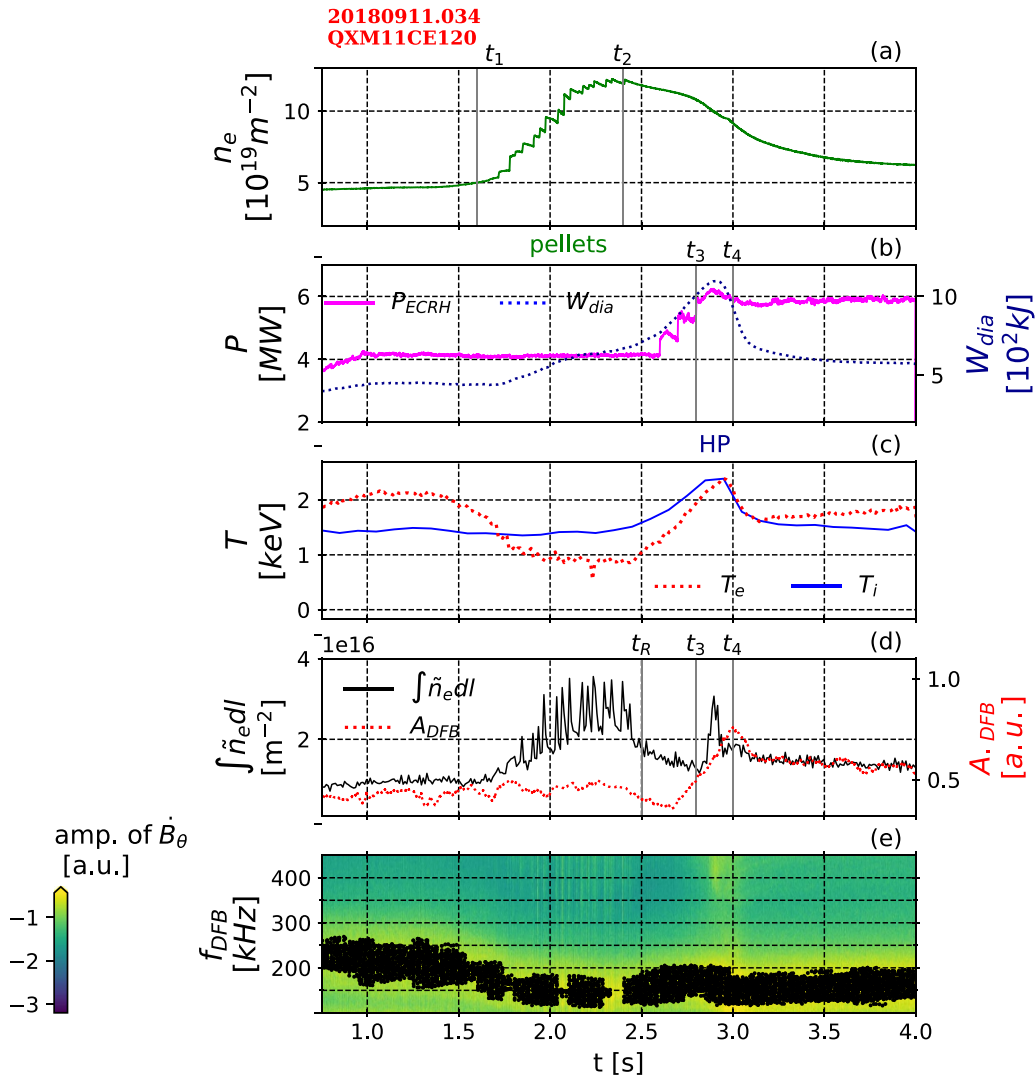


**Figure 12.** (a) For experimental discharge #20180911.034, line-averaged density,  $\int n_e dl$  (green). (b) Heating powers,  $P_{ECRH}$  (magenta) and  $P_{NBI}$  (orange), and diamagnetic energy,  $W_{dia}$  (blue). (c)  $T_e$  (red) and  $T_i$  (blue). (d)  $\int \tilde{n}_e dl$  (black), and the moving average of the amplitude of the Alfvén DFB,  $A_{DFB}$  (red). (e) Spectrogram of  $\dot{B}_{\theta}$ , with the Alfvén DFB,  $f_{DFB}(t)$ , depicted by the black circles. Frozen hydrogen pellets have been injected into the plasma between  $t_1 - t_2$ .

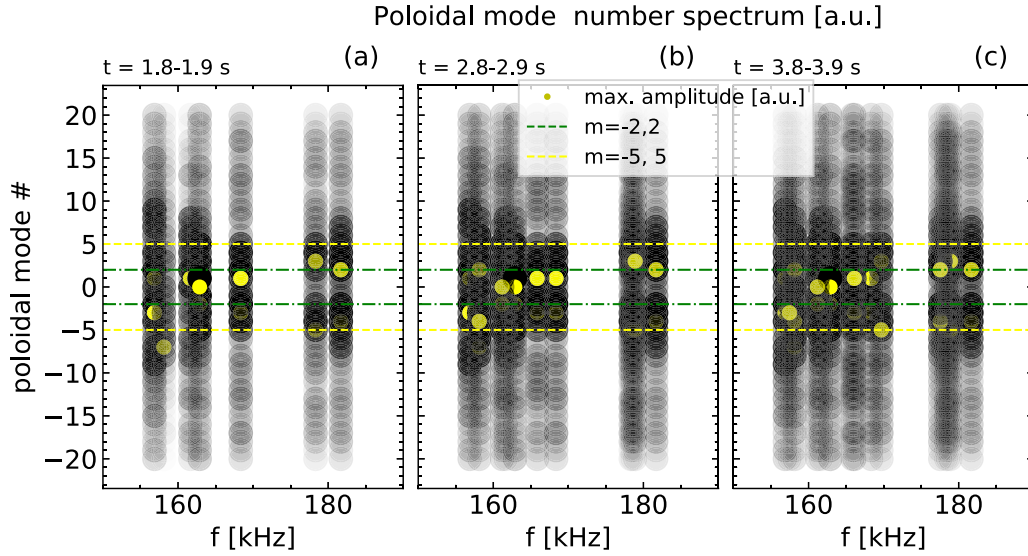


**Figure 13.** Poloidal mode spectrum computed with the SSI method, for discharge #20181011.010. The poloidal mode numbers, #, and the associated frequency of each mode are shown. The amplitudes of the different mode numbers are indicated by the intensity of the points in a.u..

is beyond the scope of this work. After the appearance of this mode  $W_{\text{dia}}$  eventually decreases and the HP phase ends. We note, that the peak of the DFB amplitude is not aligned with the peak in  $\int \tilde{n}_e dl$ , but the  $A_{\text{DFB}}$  signal corresponds to a moving averaged result. Moreover, the implemented tracking algorithm extracts maximum amplitude values in given time windows. The  $A_{\text{DFB}}$  corresponds therefore to the DFB evolution on a time averaged scale.

After the HP phase, from  $t_4$ , the energy and density decrease to slightly higher values than observed during the pre-pellet phase. Furthermore, both  $A_{\text{DFB}}$  and  $\int \tilde{n}_e dl$  also have slightly higher values after the HP phase when compared to the pre-pellet phase at  $t_1$ .

#### 4.5. Poloidal mode spectrum

Possible poloidal mode numbers associated with the DFB are identified using a Stochastic System Identification (SSI) tool [20]. This method resolves common frequency components in the data taking into account the poloidal arrangement of Mirnov coils QXM11 (see figure 1). For each frequency component resolved, SSI determines the poloidal mode numbers associated to the component. SSI resolved frequency components near the frequency values of the DFB were selected and their associated poloidal mode numbers determined. In figure 13 the poloidal mode numbers estimated from multiple Mirnov data time series are shown for a set of different mode frequencies. The frequencies were chosen around the DFB range determined during the discharge #20181011.010 (represented in figure 6(e)).

The proximity and variety of frequency components detected in the magnetic fluctuations spectra complicates the application of the SSI method. SSI does not find a single dominant mode number for the example in figure 13, but rather a

mode number range (cf. the amplitudes shown in grey scale). Throughout this example, and for other examples of OP1.2b, a systematic result of the most likely poloidal mode numbers being low and in the interval  $|m| \lesssim 5$  was concluded.

## 5. Discussion

The radial localization of the magnetic fluctuations DFBs remains undetermined and is still under investigation. The Mirnov diagnostic does not provide radial information and a precise localization of the radial position of the detected activity was neither possible from other diagnostic data. We note, that these frequency bands are not detected by the ECE or soft x-ray [7] diagnostics. ECE or soft x-ray in principle could help to clarify the radial position of the observed modes at W7-X, but the frequency domain above 100 kHz is not well resolved by these diagnostics. Previous comparisons of the poloidal mode numbers measured for the observed frequencies were in good agreement with EAEs in the continuum calculations, localized around  $r_{\text{eff}}/a \sim 0.7 - 0.8$  [32]. Despite not knowing the radial localization of the magnetic fluctuations' DFBs, their nature is successfully investigated through the DFBs dynamics. The Alfvénic nature of the DFBs is clear from the  $1/\sqrt{n_e}$  trend in figure 7.

The DFBs are similar for most configurations with the exception of the DBM (low-iota). DFBs examples for the FTM (high-iota), EJM (standard) and KJM (high-mirror) are emphasized for similar line integrated plasma densities, and we find a good agreement between the frequency of the DFBs and the EAE gap from AW continuum spectrum calculations. The DFBs determined in the DBM configuration are systematically higher than in other magnetic configurations. The difference is neither justified by the line integrated plasma density nor by the magnetic field magnitude. The centre value of the

DFB traced in a DBM example (cf figure 8(b)) is higher than the EAE gap. The lower frequency limit of the band is close to  $f = 225$  kHz, closer to the gap interval. The DFB determined by the tracking method in the DBM might not have a strong agreement with the EAE gap, but higher gaps are present in the continuum, and CFBs are observed in the frequency interval of the EAE gap, close to  $f = 180 - 220$  kHz.

A precise determination of the poloidal and toroidal mode numbers was not possible from the Mirnov diagnostic, but SSI results point to poloidal mode numbers in the range of  $|m| \leq 5$ . In several examples one is able to identify in the continuum calculations  $|m| \leq 5$  modes near the EAE gap in agreement with the experimental observations. The continuum for the example of the KJM discharge #20181011.010 has a large EAE gap in the frequency range of  $f \sim 150 - 200$  kHz. The centre of the determined DFB between  $f = 155 - 200$  kHz is consistent with the EAE gap. The DFB trace also includes points near  $f \sim 250$  kHz that we would attribute to a CFB, which would be more consistent with a higher gap in the continuum. In this example poloidal mode numbers  $|m| \leq 5$  were again identified within the dominant frequencies. Modes with  $|m| \leq 5$  could also be identified from the continuum calculations near the EAE gap.

A plasma diamagnetic energy below  $W_{\text{dia}} = 200$  kJ seems to be a threshold for the occurrence of the narrower bands with a width in the frequency range of  $\Delta f \lesssim 50$  kHz. A full investigation of the underlying mechanisms associated to this change is not covered in this work. A similar threshold between the widths of the CFBs has been observed in further data from examples during OP1.2b (not presented in figure 5). The narrower bands are relatively rare in most experiments of OP1.2b. For the majority, these bands have been identified in periods with smaller plasmas with  $W_{\text{dia}}$  below 200 kJ, where the plasma minor radius of  $a = 0.5$  m is reduced to  $a \simeq 0.3 - 0.4$  m. A possible explanation might be that fewer mode frequencies are excited during these periods of smaller volumes.

In a first example, for KJM plasma #20181011.010, we observe that the amplitude of the Alfvén DFB correlates to the ECRH power, plasma stored energy, electron temperature, and turbulence level (figure 6). The stepping down of the ECRH power is compatible with a decrease in the ITG growth rates in the KJM plasma analysed, resulting in lower turbulent density fluctuations (as proposed for [38]). Decreasing turbulence level (measured by the PCI diagnostic) is found for plasma time ranges with decreasing average  $T_e$  during a similar ECR-heated experiment in [38]. We draw the same conclusions from time points investigated in more than 700 discharges. For measurements taken for individual configurations, the amplitude of the DFBs scales with the ECRH power, plasma stored energy, and turbulence amplitude. An exception to the scaling of  $A_{\text{DFB}}$  with  $W_{\text{dia}}$  and  $P_{\text{ECRH}}$  is found during the HP discharges with peaked density profiles. The amplitude of the Alfvén DFB is reduced while the turbulent density fluctuations are reduced. The reduction of the amplitude of the Alfvén DFB is observed for similar HP experiments during the window of reduced turbulent density fluctuations, despite of the plasma stored energy increase during the same window. This scenario

during the HP experiments is clearly different to the trends in figure 10. The observation of this reduction of  $A_{\text{DFB}}$ , despite the plasma stored energy increase, suggests that  $A_{\text{DFB}}$  is mainly correlated to the turbulence amplitude. Overall the PCI measurements of turbulent density fluctuations scale with the plasma stored energy [35] in most but not all W7-X plasma phases. The general scaling of the amplitude of the Alfvén DFB with plasma stored energy in figure 10(b) seems therefore related to the scaling with the turbulence amplitude shown in figure 11. A clear configuration dependency was observed in the trends in figure 11, with higher amplitudes measured for most experiments with the high-iota FTM configuration. An explanation for the higher amplitudes observed in the FTM configurations was not found so far. One might speculate, that the intrinsic field structure in the high iota magnetic field configuration with a single poloidal edge island chain might play a role here. In contrast, KJM and EJM configurations have five separate edge islands. DBM has a single island chain similar to FTM, but at a lower iota.

## 6. Conclusions

Insights gained from implementing a new tracking algorithm on Mirnov data are a great asset to comprehending the dynamics of MHD modes and plasma behaviour at the W7-X stellarator. By confirming the Alfvénic nature of dominant plasma magnetic fluctuations for a larger data set, and identifying the correlations with different plasma parameters. No specific mode is identified in the broadband fluctuations investigated. The multi-peaked structure of the CFBs spectra suggests that we observe a broad excitation of AEs with a peak excitation at the DFB in the EAE gap. This could suggest that we are observing discrete EAEs. The amplitudes of the Alfvén DFBs are shown to have a strong correlation with the ECRH power, plasma stored energy and turbulence level. The existence of a correlation between the plasma turbulence level and the broadband mode excitation, even though the correlations between ECRH power and plasma diamagnetic energy have disappeared, indicates that an interaction with the plasma turbulence might be the cause of the broadband mode excitation. It remains difficult to infer if the effect of the heating power and higher plasma stored energy is on the AEs criteria of existence or damping within the Alfvén continuum, as for example phase-mixing damping mechanism, or on a free energy associated to plasma gradients that causes the excitation of the observed modes. One could argue that the changes introduced by the ECR heating power, and associated changes of the plasma profiles not only affect the turbulence but simultaneously the amplitude of the observed Alfvén CFBs. This hypothesis suggests that the turbulence instabilities coexist with the Alfvén waves but having no relevant interaction between each other, and are simultaneously altered by e.g. profile effects. There are several reports on the effects of localized ECRH on pre-exiting AEs (references from [15]). The single identification of one of the physical mechanisms proposed is not straightforward. Localized ECRH can modify

different properties of the AEs drive and damping mechanisms, by introducing local changes in the thermal plasma profiles (for details, see [15]). Unfortunately, the comparison of the plasma  $n_e$ ,  $T_e$  gradients for the different data analysed is not conclusive at this point. We tried comparing the profile changes through the entire length of single discharges, and to also compare the profile changes between the different discharges. The profiles obtained for  $n_e$  with the Thomson scattering diagnostic, and  $T_e$  with either the Thomson scattering or the ECE diagnostics often show a huge scattering of the data. This current problem with the accuracy of the available  $n_e$ ,  $T_e$  profiles makes it very difficult to draw conclusions of possible profile effects in correlation to the Alfvénic activity observed. A correlation between the AEs and changes in the free energy from the  $T_{e,i}$  and/or  $n_{e,i}$  gradient length profiles is not completely discarded.

EUTERPE [33] simulations considering different thermal plasma profiles of W7-X were computed to investigate the ability of the bulk plasma to destabilize potential modes in the EAE and TAE gaps. The modelling included kinetic ions and electrons, and no fast ions, which is in agreement with the experimental conditions. Under these circumstances, no unstable modes were found in the simulations, the initial perturbations (not yet eigenmodes of the system) just decayed. This result therefore is in agreement with the findings of this paper in that turbulence seems to be a required ingredient to destabilize the AEs. Especially since the damping rates obtained in the EUTERPE simulations are not very high, the potential modes are close to marginality and could be excited if some energy was transferred from the turbulence to these modes. Further numerical simulations, which are ongoing at the moment, attempt to couple AE simulations with linear ITG simulations in order to investigate this interaction numerically.

## Acknowledgments

This work has been carried out within the framework of the EUROfusion Consortium, funded by the European Union via the Euratom Research and Training Programme (Grant Agreement No 101052200 - EUROfusion). Views and opinions expressed are however those of the author(s) only and do not necessarily reflect those of the European Union or the European Commission. Neither the European Union nor the European Commission can be held responsible for them.

## Appendix .Tracking algorithm for DFBs

The Welch method [41] with fast Fourier transform analysis is implemented to compute the power spectra of the fluctuating  $\hat{B}_\theta$  signal, and the spectrogram matrix,  $S_{M \times N}$ , for the entire duration of the signal. Each location  $ij$  of the matrix  $S_{M \times N} = (s_{i,j}) \in \mathbb{R}^{M,N}$  corresponds to the PSD for a particular time window  $j$  ( $\in \mathbb{R}^N$ ) and frequency window  $i$  ( $\in \mathbb{R}^M$ ).

The matrix  $S_{M \times N}$  is divided along the  $N$  direction, by groups of  $F$  joined columns, which in the time domain corresponds to dividing  $S_{M \times N}$  in time intervals  $\Delta t_l$ . For the example

in figure 3, the spectrogram in figure 3(a) corresponds to the  $S_{M \times N}$  matrix and the temporal scale of four different  $\Delta t_l$ -iterations are represented by the black shaded areas ( $\Delta t_l = 0.1$ s, and  $l = 9, 39, 49, 77$ ). In figures 3(b)–(e),  $F = 2049$  PSD calculations are represented in function of the frequency (for the selected time ranges  $\Delta t_9$  in 3(b),  $\Delta t_{39}$  in 3(c),  $\Delta t_{49}$  in 3(d), and  $\Delta t_{77}$  in 3(e)). The  $F$  functions plotted can be pictured as  $F$  columns within the matrix  $S_{M \times N}$  illustrated in equation (A1). One function corresponds to one column of the matrix, the intensity is represented in the y-axis (PSD [a.u.]), while the frequency domain on the x-axis ( $f$  [kHz]). The PSD functions are shown in figures 3(b)–(e) for the entire frequency domain of  $S_{M \times N}$  (i.e. the entire  $M$  dimension).

For each  $\Delta t_l$  a threshold,  $A_{\text{thresh}}^l$ , is defined for the PSD values in order to distinguish and extract the dominant features of the spectrogram in that time window (for  $S^{*,l}$ ).

$$A_{\text{thresh}}^l = a \cdot \max(S^{*,l}),$$

where  $a$  [a.u.] is a constant determined to be suitable for the amplitude distribution in the spectra.

In figures 3(b)–(e), the threshold values,  $A_{\text{thresh}}^l$ , determined for each of the intervals  $\Delta t_{l=9,39,49,77}$  are represented by the red lines. During this example,  $A_{\text{thresh}}^l$  is calculated with  $a = 0.56$ .

After, the spectrogram is divided in smaller frequency intervals  $\Delta f_k$ , having now both the matrix  $S_{M \times N}$  divided along the  $N$  direction in the time intervals  $\Delta t_l$ , and along the  $M$  direction in the frequency intervals  $\Delta f_k$ . The steps until now correspond to dividing the original spectrogram,  $S_{M \times N}$ , in sub-matrices  $B_{E \times F}$  for the intervals  $(\Delta f_k, \Delta t_l)$ , as illustrated for equation (A1) by the blue shaded sub-matrix,

$$S_{M \times N} = \begin{array}{c} \begin{array}{c} B_{E \times F}^{k,l} \\ \left[ \begin{array}{cccc} s_{1,1} & s_{1,2} & \cdots & \cdots & s_{1,N} \\ s_{2,1} & s_{2,2} & \cdots & \cdots & s_{2,N} \\ \vdots & \vdots & \ddots & \ddots & \vdots \\ \vdots & \vdots & \Delta t_l & \ddots & \vdots \\ s_{M,1} & s_{M,2} & \cdots & \cdots & s_{M,N} \end{array} \right] \end{array} \\ \left. \begin{array}{c} \Delta f_k \\ \Delta t_l \end{array} \right\} \end{array} \quad \begin{array}{c} \updownarrow \\ \tau \end{array}, \quad (A1)$$

where  $k = 0, 1, \dots, \frac{M}{E} - 1$ ,  $l = 0, 1, \dots, \frac{N}{F} - 1$ , and

$$\begin{cases} \frac{M}{E} \simeq \frac{dr}{\Delta t_l} \\ \frac{N}{F} \simeq \frac{df}{\Delta f_k} \end{cases}. \quad (A2)$$

The approximations in equation (A2) are because when implementing the tracking method the different matrices  $B_{E \times F}^{k,l}$  overlap along both the  $M$  and  $N$  directions.

In each sub-matrix  $B_{E \times F}^{k,l}$  smaller intervals are used to divide it again in the  $N$  direction, i.e. in the time domain only.

The smaller intervals correspond to  $\Delta t_h$ , and one obtains the sub-matrices  $B^{k,l,h}$ , as illustrated below in equation (A3) by the red shaded sub-matrix.

$$B_{E \times F}^{k,l} = \begin{matrix} B^{k,l,h} \rightarrow A_{\max}^{kl,h} \equiv \max(B^{k,l,h}) \\ \left[ \begin{array}{cccc} s_{kE+1,1F+1} & s_{kE+1,1F+2} & \cdots & \cdots & s_{kE+1,1F+F} \\ s_{kE+2,1F+1} & s_{kE+2,1F+2} & \cdots & \cdots & s_{kE+2,1F+F} \\ \vdots & \vdots & \ddots & \ddots & \vdots \\ \vdots & \vdots & \ddots & \ddots & \vdots \\ s_{kE+E,1F+1} & s_{kE+E,1F+2} & \cdots & \cdots & s_{kE+E,1F+F} \end{array} \right] \cdot \\ \Delta t_h \end{matrix} \quad (\text{A3})$$

The maximum PSD value within each  $B^{k,l,h}$  is extracted, and represented by  $A_{\max}^{kl,h}$  as illustrated for equation (A3). Analogously, the respective time and frequency values are represented by  $t_{\max}^{kl,h}$  and  $f_{\max}^{kl,h}$ . After repeating over the entire range of index F of the sub-matrix  $B_{E \times F}^{k,l}$ , one gets the vector  $A_{\max}^{kl} = [A_{\max}^h]^{kl}$ ,  $t_{\max}^{kl} = [t_{\max}^h]^{kl}$ ,  $f_{\max}^{kl} = [f_{\max}^h]^{kl}$ , where  $h = 0, 1, \dots, \left(\frac{\Delta t_l}{\Delta t_h}\right) - 1$ .

Examples of the  $A_{\max}^{kl} = [A_{\max}^h]^{kl}$  in function of  $f_{\max}^{kl} = [f_{\max}^h]^{kl}$  are shown in figures 3(b)–(e). In figure 3(b), for example, one coloured series of circles represents the  $A_{\max}^{kl}$  determined for one  $\Delta f_k$ -iteration. A total of nine different  $\Delta f_k$ -iterations are represented in the example of figure 3(b). For each coloured trace representing  $A_{\max}^{kl}$ , an individual circle corresponds to one  $A_{\max}^{kl}$  point for different  $\Delta t_h$ -iterations. Determining the maximum as  $A_{\max}^{kl} = [A_{\max}^h]^{kl}$  in different  $\Delta f_k$  intervals allows to extract multiple frequency components with comparable amplitudes during close temporal windows of the analysis. Thereby, is resolved the band instead of a single frequency component.

The average of  $A_{\max}^{kl}$  is compared to the threshold  $A_{\text{thresh}}^l$ . The frequency components of the DFB,  $f_{\text{DFB}}(t)$ , are determined as follows,

$$\begin{cases} f_{\text{DFB}}^{kl} \equiv f_{\max}^{kl} & \text{if } \langle A_{\max}^{kl} \rangle > A_{\text{thresh}}^l \\ f_{\text{DFB}}^{kl} \equiv 0 & \text{if } \langle A_{\max}^{kl} \rangle < A_{\text{thresh}}^l \end{cases} \quad (\text{A4})$$

In figure 3(d) also nine different  $\Delta f_k$ -iterations are presented, while in figures 3(c) and (e) four different  $\Delta f_k$ -iterations are presented. Every  $A_{\max}^{kl}$  coloured trace has 6 points for this example, where  $\Delta t_l = 0.1\text{ s}$  and  $\Delta f_k = 5\text{ kHz}$ . The represented nine (figures 3(b) and (e)) and four (figures 3(c) and (d))  $\Delta f_k$ -iterations correspond to the cases where the average values of  $A_{\max}^{kl}$  surpass the defined threshold  $A_{\text{thresh}}^l$ . All the  $f_{\text{DFB}}^{kl}$  vectors evaluated for the entire time and frequency domain of the spectrogram in figure 3(a) are joined into the  $M, N$ -dimensional  $f_{\text{DFB}}(t)$  band. This last step is illustrated from figure 3(d) to an instance of 3(f). The final result for the example in figure 3(a)

is shown in figure 3(f). The respective amplitude of the final DFB result over time is shown in grey scale in figure 3(f).

## ORCID iDs

K. Rahbarnia  <https://orcid.org/0000-0002-5550-1801>  
 J. Schilling  <https://orcid.org/0000-0002-6363-6554>  
 R. Kleiber  <https://orcid.org/0000-0002-2261-2855>  
 A. Könies  <https://orcid.org/0000-0003-4306-9000>  
 T. Sunn Pedersen  <https://orcid.org/0000-0002-9720-1276>

## References

- [1] Äkäslompolo S. et al 2019 Validating the ascot modelling of NBI fast ions in Wendelstein 7-X stellarator *J. Instrum.* **14** C10012
- [2] Böhner J.-P. et al 2021 Phase contrast imaging measurements and numerical simulations of turbulent density fluctuations in gas-fuelled ECRH discharges in Wendelstein 7-X *J. Plasma Phys.* **87** 905870314
- [3] Baldzuhn J. et al 2019 Pellet fueling experiments in Wendelstein 7-X *Plasma Phys. Control. Fusion* **61** 095012
- [4] Baldzuhn J. et al 2020 Enhanced energy confinement after series of pellets in Wendelstein 7-X *Plasma Phys. Control. Fusion* **62** 055012
- [5] Beidler C.D. et al 2021 Demonstration of reduced neoclassical energy transport in Wendelstein 7-X *Nature* **596** 221–6
- [6] Bozhnikov S.A. et al 2020 High-performance plasmas after pellet injections in Wendelstein 7-X *Nucl. Fusion* **60** 066011
- [7] Brandt C. et al 2020 Soft x-ray tomography measurements in the Wendelstein 7-X stellarator *Plasma Phys. Control. Fusion* **62** 035010
- [8] Brunner K.J., Akiyama T., Hirsch M., Knauer J., Kornejew P., Kursinski B., Laqua H., Meineke J., Trimino Mora H. and Wolf R.C. 2018 Real-time dispersion interferometry for density feedback in fusion devices *J. Instrum.* **13** 09002
- [9] Cheng C.Z. and Chance M.S. 1986 Low-n shear Alfvén spectra in axisymmetric toroidal plasmas *Phys. Fluids* **29** 3695–701
- [10] Dewar R.L., Grimm R.C., Johnson J.L., Frieman E.A., Greene J.M. and Rutherford P.H. 1974 Long-wavelength kink instabilities in low-pressure, uniform axial current, cylindrical plasmas with elliptic cross sections *Phys. Fluids* **17** 930–8
- [11] Duong H.H., Heidbrink W.W., Strait E.J., Petrie T.W., Lee R., Moyer R.A. and Watkins J.G. 1993 Loss of energetic beam ions during TAE instabilities *Nucl. Fusion* **33** 749
- [12] Edlund E.M., Porkolab M., Huang Z., Grulke O., Böttger L.-G., von Sehren C. and von Stechow A. 2018 Overview of the Wendelstein 7-X phase contrast imaging diagnostic *Rev. Sci. Instrum.* **89** 10E105
- [13] Endler M. et al 2015 Engineering design for the magnetic diagnostics of Wendelstein 7-X *Fusion Eng. Des.* **100** 468–94
- [14] Fredrickson E.D. et al 2003 Wave driven fast ion loss in the national spherical torus experiment *Phys. Plasmas* **10** 2852–62
- [15] Garcia-Munoz M. et al 2019 Active control of Alfvén eigenmodes in magnetically confined toroidal plasmas *Plasma Phys. Control. Fusion* **61** 054007
- [16] Geiger B. et al 2020 Observation of Alfvén eigenmodes driven by off-axis neutral beam injection in the TCX tokamak *Plasma Phys. Control. Fusion* **62** 095017
- [17] Huang Z., Edlund E., Porkolab M., Böhner J.P., Böttger L.-G., von Sehren C., von Stechow A. and Grulke O. 2021 The

- Wendelstein 7-X phase contrast imaging diagnostic *J. Instrum.* **16** 01014
- [18] Jiménez-Gómez R. *et al* 2011 Alfvén eigenmodes measured in the TJ-II stellarator *Nucl. Fusion* **51** 033001
- [19] Kieras C.E. and Tataronis J.A. 1982 The shear Alfvén continuous spectrum of axisymmetric toroidal equilibria in the large aspect ratio limit *J. Plasma Phys.* **28** 395–414
- [20] Kleiber R., Borchardt M., Könies A. and Slaby C. 2021 Modern methods of signal processing applied to gyrokinetic simulations *Plasma Phys. Control. Fusion* **63** 035017
- [21] Klinger T. *et al* 2019 Overview of first Wendelstein 7-X high-performance operation *Nucl. Fusion* **59** 112004
- [22] Klinger T. *et al* 2013 Towards assembly completion and preparation of experimental campaigns of Wendelstein 7-X in the perspective of a path to a stellarator fusion power plant *Fusion Eng. Des.* **88** 461–5
- [23] Könies A. and Eremin D. 2010 Coupling of Alfvén and sound waves in stellarator plasmas *Phys. Plasmas* **17** 012107
- [24] Maraschek M., Günter S., Kass T., Scott B. and Zohm H. (ASDEX Upgrade Team) 1997 Observation of toroidicity-induced Alfvén eigenmodes in ohmically heated plasmas by drift wave excitation *Phys. Rev. Lett.* **79** 4186
- [25] Melnikov A.V. *et al* 2012 Alfvén eigenmode properties and dynamics in the TJ-II stellarator *Nucl. Fusion* **52** 123004
- [26] Neuner U. *et al* 2021 Measurements of the parameter dependencies of the bootstrap current in the W7-X stellarator *Nucl. Fusion* **61** 036024
- [27] Ongena J. *et al* 2014 Study and design of the ion cyclotron resonance heating system for the stellarator Wendelstein 7-X *Phys. Plasmas* **21** 061514
- [28] Osakabe M., Yamamoto S., Toi K., Takeiri Y., Sakakibara S., Nagaoka K., Tanaka K. and Narihara K. (The LHD Experimental Group) 2006 Experimental observations of enhanced radial transport of energetic particles with Alfvén eigenmode on the LHD *Nucl. Fusion* **46** S911
- [29] Pablant N.A. *et al* 2014 Measurement of core plasma temperature and rotation on W7-X made available by the x-ray imaging crystal spectrometer (XICS) *Technical Report* (Princeton Plasma Physics Lab.(PPPL))
- [30] Petrov Y.V., Bakharev N.N., Gusev V.K., Minaev V.B., Kornev V.A., Kurskiev G.S., Patrov M.I., Sakharov N.V., Yu Tolstyakov S. and Shchegolev P.B. 2015 Effect of toroidal Alfvén eigenmodes on fast particle confinement in the spherical tokamak globus-m *J. Plasma Phys.* **81** 515810601
- [31] Rahbarnia K. *et al* 2018 Diamagnetic energy measurement during the first operational phase at the Wendelstein 7-X stellarator *Nucl. Fusion* **58** 096010
- [32] Rahbarnia K. *et al* 2020 Alfvénic fluctuations measured by in-vessel Mirnov coils at the Wendelstein 7-X stellarator *Plasma Phys. Control. Fusion* **63** 015005
- [33] Sánchez E. *et al* 2020 Nonlinear gyrokinetic PIC simulations in stellarators with the code EUTERPE *J. Plasma Phys.* **86** 855860501
- [34] Slaby C. *et al* 2020 Investigation of mode activity in NBI-heated experiments of Wendelstein 7-X *Nucl. Fusion* **60** 112004
- [35] Stechow A.V. *et al* 2020 Suppression of core turbulence by profile shaping in Wendelstein 7-X (arXiv:2010.02160)
- [36] Van Zeeland M.A. *et al* 2012 Alfvén eigenmode stability and fast ion loss in DIII-D and ITER reversed magnetic shear plasmas *Nucl. Fusion* **52** 094023
- [37] Van Zeeland M.A. *et al* 2011 Measurements and modeling of Alfvén eigenmode induced fast ion transport and loss in DIII-D and ASDEX Upgrade *Phys. Plasmas* **18** 056114
- [38] Wegner T. *et al* 2020 Impact of the temperature ratio on turbulent impurity transport in Wendelstein 7-X *Nucl. Fusion* **60** 124004
- [39] Th Wegner B.G. *et al* 2018 Design, capabilities and first results of the new laser blow-off system on Wendelstein 7-X *Rev. Sci. Instrum.* **89** 073505
- [40] Weir G *et al* 2016 43rd EPS Conf. on Plasma Physics (Leuven, Belgium, 4–8 July 2016) p 4.009 (available at: <https://kuleuvencongres.be/eps2016>)
- [41] Welch P. 1967 The use of fast Fourier transform for the estimation of power spectra: a method based on time averaging over short, modified periodograms *IEEE Trans. Audio Electroacoust.* **15** 70–73
- [42] Zegenhagen S. 2006 Destabilization of Alfvén eigenmodes by fast particles in W7-AS *PhD Thesis*